JACS
JOURNAL OF THE AMERICAN CHEMICAL SOCIETY

Article

pubs.acs.org/JACS

High-Performance Ionic Diode Membrane for Salinity Gradient Power Generation

Jun Gao,[†] Wei Guo,*[,†,∥] Dan Feng,[‡] Huanting Wang,[§] Dongyuan Zhao,*[,‡] and Lei Jiang*[,†]

[†]Beijing National Laboratory for Molecular Sciences (BNLMS), Key Laboratory of Organic Solids, Institute of Chemistry, Chinese Academy of Sciences, Beijing 100190, P. R. China

[‡]Department of Chemistry and Shanghai Key Laboratory of Molecular Catalysis and Innovative Materials, Fudan University, Shanghai 200433, P. R. China

[∥]Laboratory of Bio-inspired Smart Interface Science, Technical Institute of Physics and Chemistry, Chinese Academy of Sciences, Beijing 100190, P. R. China

[§]Department of Chemical Engineering, Monash University, Clayton, Victoria 3800, Australia

Supporting Information

ABSTRACT: Salinity difference between seawater and river water is a sustainable energy resource that catches eyes of the public and the investors in the background of energy crisis. To capture this energy, interdisciplinary efforts from chemistry, materials science, environmental science, and nanotechnology have been made to create efficient and economically viable energy conversion methods and materials. Beyond conventional membrane-based processes, technological breakthroughs in harvesting salinity gradient power from natural waters are expected to emerge from the novel fluidic transport phenomena on the nanoscale. A major challenge toward real-world applications is to extrapolate existing single-channel devices to macroscopic materials. Here, we report a membrane-scale nanofluidic device with asymmetric structure, chemical composition, and surface charge polarity, termed ionic diode membrane (IDM), for harvesting electric power from salinity gradient. The IDM comprises heterojunctions between mesoporous carbon (pore size ∼7 nm, negatively charged) and macroporous alumina (pore size ∼80 nm, positively charged). The meso-/macroporous membrane rectifies the ionic current with distinctly high ratio of ca. 450 and keeps on rectifying in high-concentration electrolytes, even in saturated solution. The selective and rectified ion transport furthermore sheds light on salinity-gradient power generation. By mixing artificial seawater and river water through the IDM, substantially high power density of up to 3.46 W/m^2 is discovered, which largely outperforms some commercial ion-exchange membranes. A theoretical model based on coupled Poisson and Nernst−Planck equations is established to quantitatively explain the experimental observations and get insights into the underlying mechanism. The macroscopic and asymmetric nanofluidic structure anticipates wide potentials for sustainable power generation, water purification, and desalination.

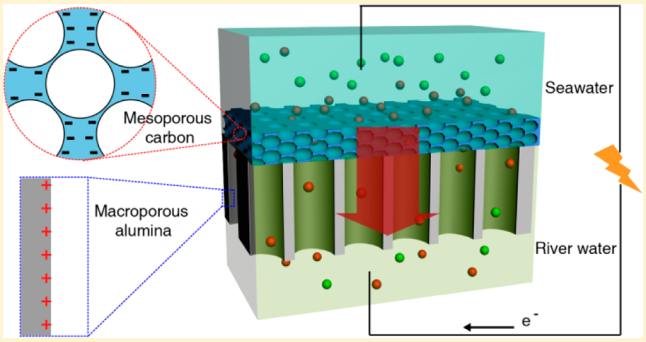

INTRODUCTION

Salinity difference between seawater and river water is a sustainable energy resource that catches eyes of the public and the investors in the background of energy crisis.[1,2] To capture this energy, interdisciplinary efforts from chemistry, materials science, environmental science, and nanotechnology have been made to create efficient energy conversion methods and materials.[3−6] Through membrane-based processes, such as reverse electrodialysis and pressure retarted osmosis, electric power can be harnessed from natural waters.[7−9] However, current membrane materials suffer from deteriorated ion selectivity, inadequate mass transportation, and hence, economically unviable power density.[10,11] Technological breakthroughs are expected to emerge from the novel fluidic transport phenomena on the nanoscale.[12,13] An orders-of-magnitude promotion in harvesting salinity gradient power can be expected from biomimetic single nanopores due to high ionic flux and surface charge density.[14−16]

To fully govern the ion transport in high-concentration electrolytes for practical salinity gradient power generation (for example, ∼0.5 M in seawater), the characteristic length scale of the fluidic system should be further reduced down to sub-10 nm and the device should be capable of mass production.[17−20] However, this requirement can hardly be met with existing single-channel nanofluidic devices, because their fabrication process highly relies on expensive scientific equipment and sophisticated material processing steps.[21] A major challenge is

Received: April 14, 2014
Published: August 19, 2014

   dx.doi.org/10.1021/ja503692z | J. Am. Chem. Soc. 2014, 136, 12265−12272

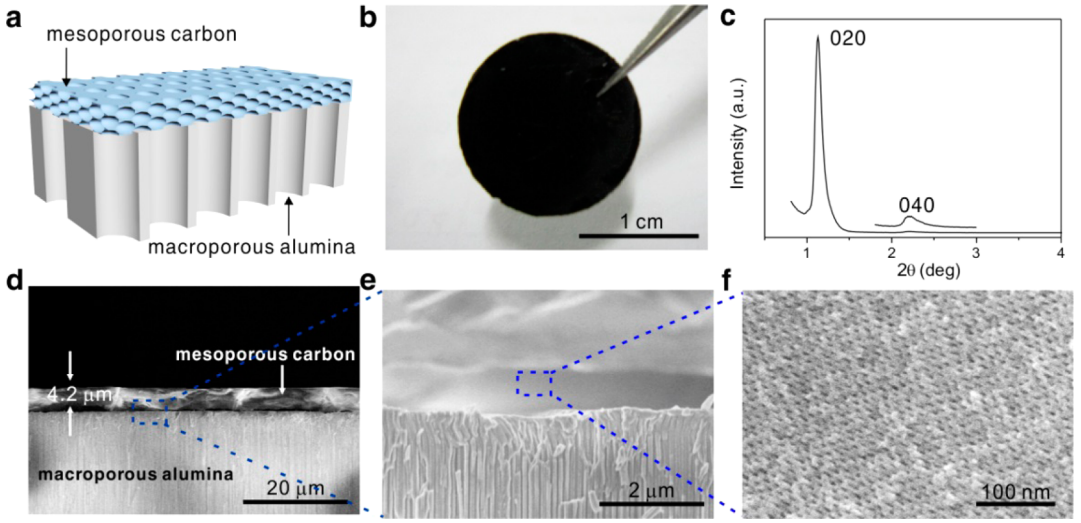

Figure 1. Meso-/macroporous heterostructured membrane. (a) Schematic illustration of the porous heterojunction between negatively charged mesoporous carbon (MesoC) and positively charged macroporous alumina (MacroA) films. (b) The lateral size of the membrane is about 1.5 cm. (c) XRD results show a cubic mesostructure (space group *Fmmm*) of the MesoC layer. (d) SEM image of the membrane cross section reveals a 4.2-μm-thick MesoC layer is on the top of a MacroA membrane. (e and f) Magnified views of the membrane show highly regular pore structure in both the MesoC and MacroA layers. The pore size of MacroA is 84 ± 16 nm. The peak diameter of MesoC is ~6.7 nm determined by nitrogen sorption test (Supporting Information Figure S3).

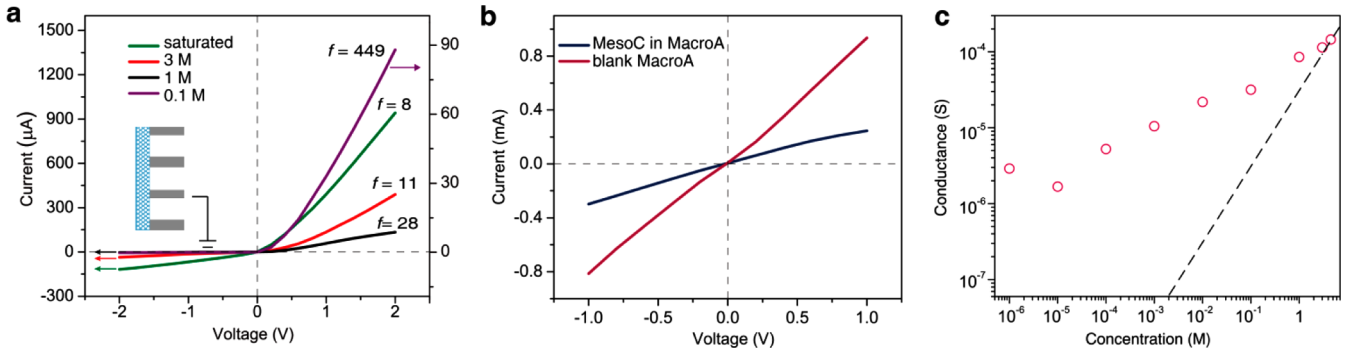

Figure 2. Highly rectified ion transport through the ionic diode membrane (IDM). (a) The nanofluidic IDM shows distinctly strong ionic rectification at high concentrations, even in saturated solution. The highest rectification ratio found in 0.1 M KCl is 449. (b) In contrast, separate macroporous alumina (MacroA) film or mesoporous carbon (MesoC) filled MacroA film show nonrectified current−voltage responses. (c) The transmembrane ionic conductance (circles) apparently deviates from bulk value (dashed line) from below ~1 M, indicating a fully surface-charge-governed ion transport.

to extrapolate these nanosized, single-channel devices to macroscopic materials.[22−26] In this context, mesoporous materials, with highly uniform pore size of typically several nanometers, high specific surface area, and simple fabrication methods,[27−29] become the ideal material component to upgrade current salinity gradient power systems.

Here, we report a membrane-scale nanofluidic device with asymmetric structure, chemical composition, and surface charge polarity, termed ionic diode membrane (IDM), for harvesting electric power from salinity gradient (Supporting Information Figure S1). The IDM comprises heterojunctions between mesoporous carbon (MesoC, pore size ~7 nm, negatively charged) and macroporous alumina (MacroA, pore size ~80 nm, positively charged). The meso-/macroporous membrane rectifies the ionic current with distinctly high ratio of ca. 450 and keeps on rectifying in high-concentration electrolytes. Experimental and calculated results prove that the introduction of structural, chemical, and electrostatic asymmetries into the nanofluidic structure selectively and preferentially facilitates the cation transport from MesoC to MacroA, and consequently results in a substantially high power density of up to 3.46 W/m^2 of membrane area by mixing artificial seawater and river water through the IDM, which largely outperforms some commercial ion-exchange membranes. The macroscopic and asymmetric nanofluidic structure anticipates wide potentials for sustainable power generation, water purification, and desalination.

■ RESULTS AND DISCUSSION

Figure 1a shows the schematic illustration of the IDM composed of a thin layer of MesoC on the top of MacroA substrate. To fabricate the heterostructured membrane, MesoC precursor was first coated onto the MacroA (Supporting Information and Figure S2). Then ordered MesoC was synthesized via evaporation induced self-assembly.[30] To prevent the precursor from penetrating into the alumina pores, a sacrificial layer of poly(methyl methacrylate) was filled into the MacroA beforehand and was completely decomposed during carbonization (Supporting Information and Figure S3). The lateral size of the IDM is about 1.5 cm (Figure 1b). Scanning electron microscopy (SEM) observation of the

dx.doi.org/10.1021/ja503692z | J. Am. Chem. Soc. 2014, 136, 12265−12272

membrane cross section shows that a 4.2-μm-thick MesoC layer is attached on the top of a 60-μm-thick MacroA substrate (Figure 1d). The diameter of the MacroA pores is 84 ± 16 nm (Figure 1e). Highly regular nanopore array is observed in the MesoC area (Figure 1f), which exhibits cubic mesostructure (space group *Fmmm*)[31] characterized by X-ray diffraction (XRD, Figure 1c). The MesoC has small peak diameter of ~6.7 nm and large specific surface area of 499 m^2 g^{-1} determined by nitrogen sorption experiment (Supporting Information and Figure S3).

At various electrolyte concentrations, the heterostructured membrane exhibits diode-like current–voltage response showing strong ionic rectification (Figure 2a). A maximum rectification ratio (f) of up to 449 is found in 0.1 M KCl solution, which is the highest value ever reported in ionic rectifying systems.[32] Of note, the IDM keeps on rectifying in high-concentration electrolytes. Even in saturated solution, f reaches 8. This result is distinct from previous reports that the ionic rectification fails in high-concentration range.[33] In contrast, the unmodified MacroA film and the MesoC filled MacroA film show no apparent rectification effect (Figure 2b). To understand these results, we test the ionic conductance of the meso-/macroporous membrane with respect to the ionic concentration (Figure 2c). The transmembrane ionic conductance remarkably deviates from bulk value from below 1 M, indicating that the ion transport through the IDM is fully surface-charge-governed,[34] even in high-concentration electrolyte.

To test the ion selectivity of the bipolar membrane, electrolyte solutions with different concentrations are placed on the two sides of the membrane. The concentration on MesoC side (c_{MesoC}) was 0.1 M and the concentration on MacroA side (c_{MacroA}) was 1 μM (red line and upper insert in Figure 3). Since c_{MesoC} is 10^5 times higher than c_{MacroA}, the ion

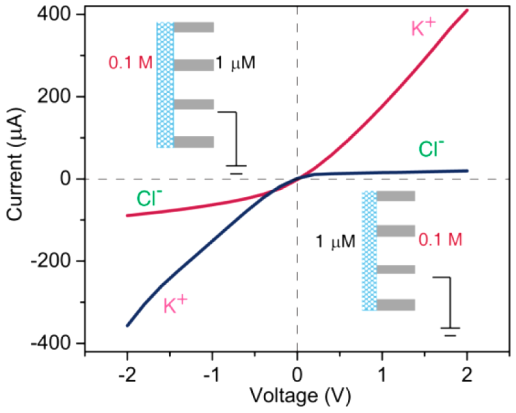

Figure 3. Ion selectivity of the IDM is verified by the ionic conductance measurements under extremely high concentration ratio. With concentrated electrolyte placed on MesoC side (red curve), the K^+ currents (at positive bias) are much larger than the Cl^- currents (at negative bias), showing strong cation selectivity. For the reversed concentration gradient (blue curve), similar conclusion can be reached.

migration from MacroA side does not contribute decisively to the measured ionic current. To a good approximation, we can compare the ionic currents carried by cations or by anions, separately.[35] Compared with the Cl^- current (at negative potential), the substantially enhanced K^+ current (at positive potential) suggests strong cation selectivity. Moreover, we switched the electrolyte concentrations on the two sides of IDM (blue line and lower inset in Figure 3). The cation selectivity can be also verified by the much higher K^+ current (at negative potential) than the Cl^- current (at positive potential). Note that the K^+ conductivity in the former case is 15.2% higher than that in the latter case. This evidence suggests that the ion transport through the IDM is directionally asymmetric. There exists a preferential direction for cation transport from the MesoC side toward the MacroA side.

The MesoC part is negatively charged and the MacroA carries positive surface charge in neutral or acidic solutions. Hence, in the IDM, the MacroA layer does not function merely as a solid support, it forms charge heterojunction with the MesoC layer (Figure 4). On the whole, the ion selectivity of the IDM is dominated by the MesoC layer due to the narrow pore size (Supporting Information Figure S4). The introduction of both electrostatic, chemical, and structural heterostructures makes the transmembrane ionic current highly rectified.[6]

This hypothesis can be quantitatively supported by a theoretical model based on coupled Poisson and Nernst–Planck (PNP) equations (Supporting Information and Figure S5). The separate MesoC film (channel width is 4 nm) does not rectify the ionic current (Figure 5a and 5b). After a wide segment is introduced on one end (channel width is 60 nm), the ionic current through the hybrid nanofluidic channels becomes rectified ($f \approx 14$). If the wide segment takes opposite surface charge, highly rectified ionic current can be observed ($f \approx 232$) due to the remarkable ion-enrichment and depletion at the meso/macro interface under the opposite electric potentials. When the length percentage of the MesoC channel reaches an optimal value of 20%–40%, the highest rectification ratio approaches 300 (Figure 5c). In addition, the chemical composition of the heterojunction structure provides an extremely sharp transition zone between the negatively and positively charged parts that also accounts for the very large rectification ratio.[36] In short, by sequentially introducing structural, electrostatic, and length asymmetries, the rectification ratio is enlarged stepwisely. The rectification ratio can be further increased with the channel length in MesoC film (Figure 5d). Therefore, the experimentally observed strong rectification effect can be rationally expected.

The selective and rectified ion transport sheds further light on salinity gradient power generation. We mount the IDM into a two-compartment electrochemical cell (Figure 6a). The testing membrane area is 0.03 mm^2. Under a salinity gradient, for example, c_{MesoC}/c_{MacroA} = 0.1 M/1 μM, the open-circuit voltage (U_{OC}) and short-circuit current (I_{SC}) are read from the intercepts on the voltage and current axes (Figure 6b). The contribution from the redox potential on the electrodes is readily subtracted through subsequent data analysis (Supporting Information Figure S6 and Table S1). Under reversed salinity gradient from MesoC to MacroA, the internal resistance of the nanofluidic power source is reduced by 53%, owing to the preferential direction for cation transport.[37] Hence, in the following tests, the concentration on the MesoC side was kept high. The generation of U_{OC} and I_{SC} is also verified by the PNP model in various conditions (Supporting Information Figure S7).

We further test the power generation from the IDM under a series of concentration gradient. We set c_{MacroA} = 1 μM and gradually elevate c_{MesoC} from 1 μM to 3 M. Both U_{OC} and I_{SC} increase with the concentration gradient (Figure 6c). Typically, the U_{OC} is several tens to more than 100 mV, and the maximum current density reaches 98.8 A/m^2. The energy

dx.doi.org/10.1021/ja503692z | J. Am. Chem. Soc. 2014, 136, 12265–12272

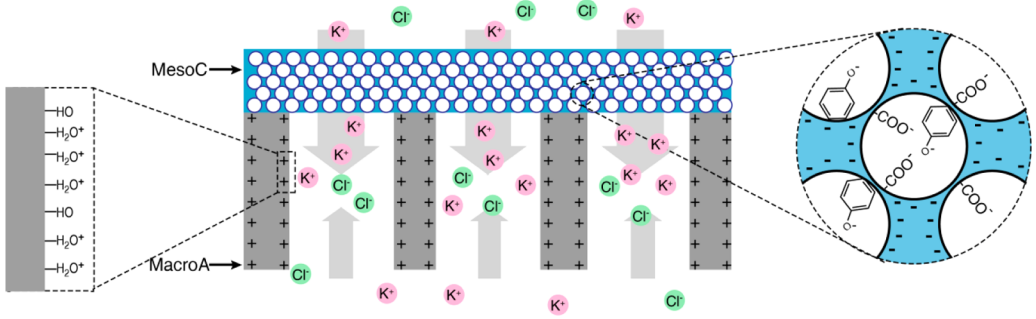

Figure 4. Schematic of the MesoC/MacroA heterojunction structure. The MesoC carries negative charge and it is cation-selective (wide gray arrows). The MacroA carries positive charge and it is anion-selective (narrow gray arrows). On the whole, owing to the narrow pore size of the MesoC, the ion selectivity of the entire membrane is dominated by the MesoC layer.

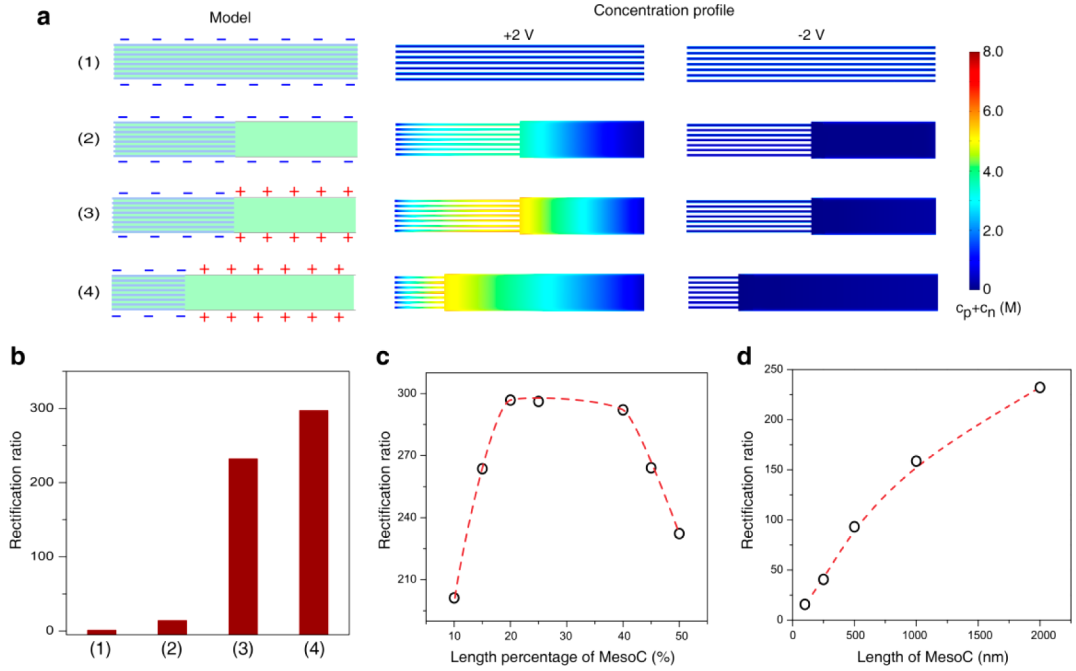

Figure 5. Numerical simulation of the highly rectified nanofluidic IDM. (a and b) The calculated ion concentration profile inside the nanochannels reveals that the ultrahigh ionic rectification results from the remarkable ion concentration enrichment at positive voltage bias and depletion at negative voltage bias. Among four types of 2D configuration, symmetric nanochannels do not rectify ionic current (1). By sequentially introducing structural (2), electrostatic (3), and length asymmetries (4), the rectification ratio is increased stepwisely. (c) The total length of the MesoC/MacroA nanochannel is set to be 4000 nm. The maximum rectification ratio is found when the percentage of MesoC part approaches 20%−40%. (d) The calculated rectification ratio increases with the length of MesoC. The length percentage of the MesoC is set to be 50%. All the calculation parameters are listed in Supporting Information Tables S2 and S3.

conversion efficiency declines with the concentration gradient from 26.4% to 5.7% (Supporting Information Figure S8). The generated power can be output to external circuit to supply an electronic load (Figure 6d). Then, the electric power (P_R) consumed on the resistor load (R_L) in the external circuit can be directly obtained by $P_R = I^2 \times R_L$. When artificial seawater (0.5 M NaCl) and river water (0.01 M NaCl) are mixed, with the increase of load resistance, the diffusion current gradually decreases, but the output power reaches its peak value when the load resistance is ∼10 kΩ. The maximum power density reaches 3.46 W/m^2 with an efficiency of 37.3% (Supporting Information). We also test the power generation from other two types of IDM with varied pore size of ca. 23 and 33 nm on the MesoC side (FDU-18, Supporting Information). The maximum output power density decreases with the pore size of MesoC from 7 to 33 nm (Supporting Information Figure S9). This is because, for larger pore width, the surface-governed property is less dominant.

The generation of electric current under salinity gradient lies in the ion selectivity of the bipolar membrane channels. Theoretical calculations are performed based on the above-mentioned PNP model. Detailed calculation parameters can be found in Supporting Information Table S4. The symmetric nanofluidic diodes with equal pore size, channel length, and surface charge density of positive and negative zones are not ion-selective.[38] But strong cation selectivity is achieved by the nanofluidic IDM with structural, chemical, and electrostatic asymmetries (Figure 7a). Quantified via the cation transference numbers (Supporting Information),[39] the ion selectivity of the IDM is dominated by the charge properties on the MesoC part with narrow pore size. By fixing the charge density on MesoC (−0.06 C/m^2) and varying the charge density on MacroA, the

dx.doi.org/10.1021/ja503692z | J. Am. Chem. Soc. 2014, 136, 12265−12272

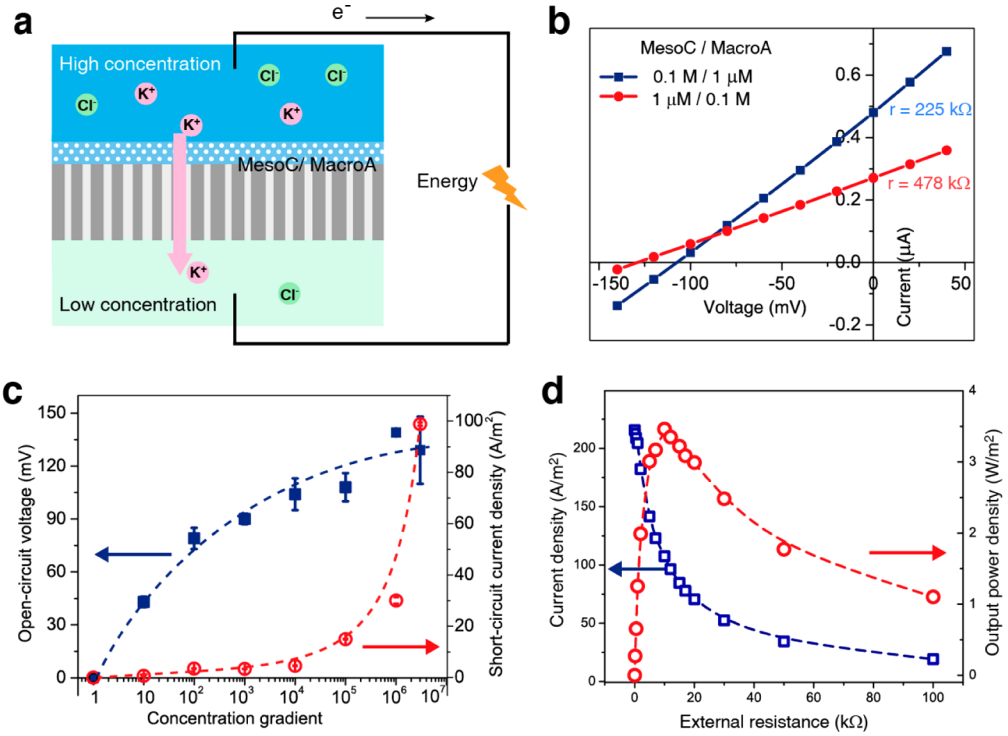

Figure 6. Energy conversion from salinity difference. (a) Schematic illustration of the energy harvesting under concentration gradient. (b) For c_{MesoC} = 0.1 M and c_{MacroA} = 1 μM, the U_{OC} and I_{SC} are 108 mV and 0.48 μA (blue). If the concentration gradient is reversed (red), they are 129 mV and 0.27 μA (red). The enhanced ion diffusion from MesoC toward MacroA reduces the internal resistance (r) of the nanofluidic system by nearly 53%. (c) The I_{SC} (open) and U_{OC} (solid) are measured in a series of concentration gradient. The concentration on MacroA side is fixed at 1 μM. Both I_{SC} and U_{OC} increase with the salinity gradient. (d) The generated power can be output to external circuit and supply an electronic load. By mixing artificial seawater (0.5 M NaCl) and river water (0.01 M NaCl), the output power density reaches its peak value of 3.46 W/m^2 at the resistance of ~10 kΩ.

calculated cation transference number keeps around 0.8, showing strong cation-selectivity. This result is also confirmed by the selective permeation of charged fluorescent dyes (Supporting Information Figure S10). On the contrary, if we fix the charge density on MacroA (0.06 C/m^2) and vary the charge density on MesoC, the cation transference number can be tuned in a much wide range from 0.77 (cation-selectivity) to 0.18 (anion-selectivity). In some cases, for example, if the surface charge density of MacroA exceeds ca. 0.03 C/m^2, the presence of a positively charged MacroA segment on the end of MesoC facilitates the generation of net diffusion current and promotes the selectivity of the device (Figure 7b). Below this value, the counterionic MacroA may reduce the overall selectivity of the IDM.

Furthermore, the asymmetric pore structure and the bipolar charge distribution help to suppress the concentration polarization, especially at the low-concentration side.[40] We compare the ion concentration profile of two types of membrane channel at the low-concentration side (Figure 7c). The first membrane type (membrane 1#) is composed of 4 nm-wide nanochannel arrays. The nanochannels are negatively charged on their inner and outter surface. The length of individual nanochannel is 4000 nm. The second membrane type (membrane 2#) is a model IDM containing structural and electrostatic heterojunctions. The small channel width is also 4 nm and the large channel width is 60 nm. From the profiles of cation concentration at the orifice on the low-concentration side, one can note that strong concentration polarization takes place in membrane 1#, for the ion concentration at the channel orifice significantly deviates from the bulk value. While for membrane 2#, the concentration polarization effect is largely suppressed. The ion concentration is only slightly higher than the bulk concentration. Therefore, the presence of positively charged segment on the low-concentration side effectively prevents the accumulation of cations, which is conductive to the generation of net diffusion current under salinity gradient.[40] The calculation results on membrane 1# also show some implications in the case of ion-exchange membranes.[41] The symmetric narrow nanochannels provide higher selectivity, and consequently higher energy conversion efficiency, but the narrow pore size restricts the throughput of the traversing ionic flow and induces severe concentration polarization. Therefore, the influence of concentration polarization phenomena can be rationally minimized by physical and chemical design of the channel structures.

For comparison, four types of commercially available cation-exchange membranes, including Nafion, Ionsep, CMI, and FKS, were tested under identical experimental conditions (Supporting Information). Although the energy conversion efficiency is not as high as that in those ion-exchange membranes, the nanofluidic IDM substantially promotes the power density (Table 1). In classic ion-exchange membranes, the size of the ionic species is comparable to the channel width (typically less than 1 nm), so that the ion transport through such membrane channels encounters great steric hindrance, resulting in low ionic conductivity.[42] For a nanopore that is wide enough to overlook these nonelectrostatic interactions between the mobile ions and the pore wall, such as the nanochannels in the IDM, the transmembrane ionic conductance can be greatly enhanced, leading to high ionic flux. Due to the large channel

dx.doi.org/10.1021/ja503692z | J. Am. Chem. Soc. 2014, 136, 12265−12272

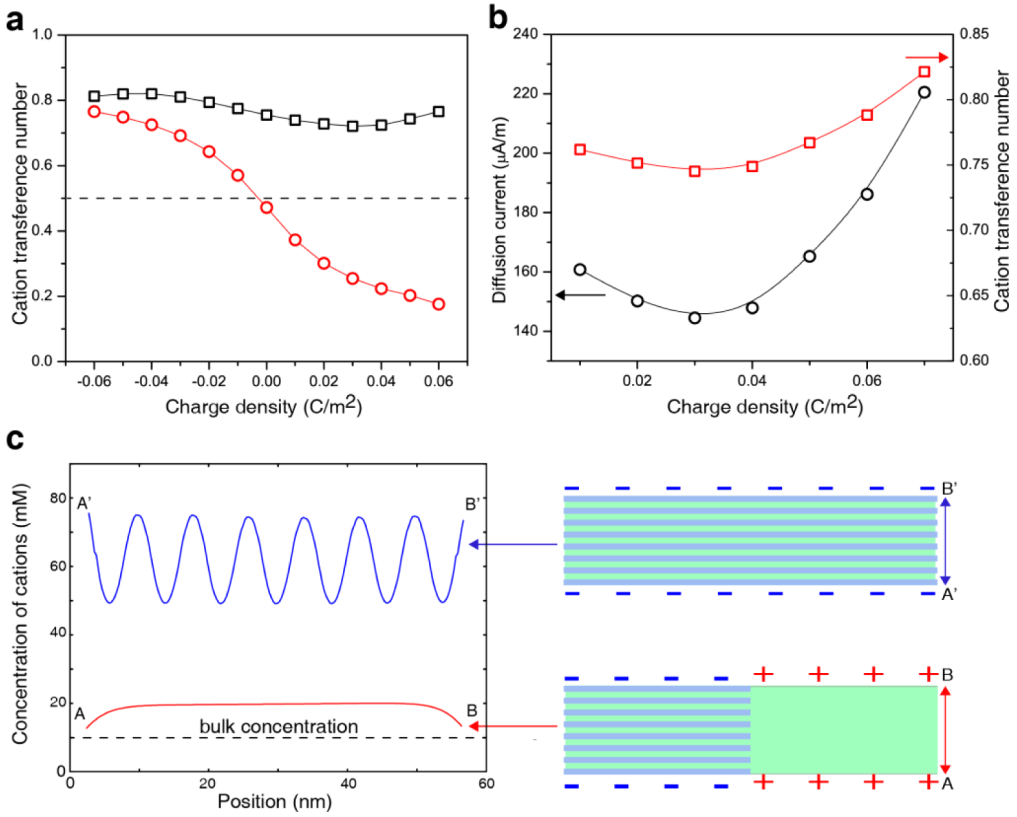

Figure 7. Numerical simulation of the energy conversion. (a) Ion selectivity of the IDM is dominated by the charge properties on the MesoC part. By fixing the charge density on MesoC to be −0.06 C/m^2 and varying the charge density on MacroA (□), we find the calculated cation transference number to be around 0.8 (cation-selectivity). On the contrary, if the charge density on MacroA is fixed to be 0.06 C/m^2 and varies the charge density on MesoC (○), the cation transference number can be tuned in a much wide range from 0.77 (cation-selectivity) to 0.18 (anion-selectivity). (b) The presence of a positively charged MacroA segment on the end of MesoC facilitates the generation of diffusion current at high charge density over 0.03 C/m^2. Below this value, the counterionic MacroA reduces the overall selectivity of the IDM. (c) The bipolar channel structure helps to suppress the ion concentration polarization on the low-concentration side. The concentration profile near the channel orifice indicates that membrane 1# (up, negatively charged 4 nm channel array) shows strong concentration polarization (largely enhanced ionic strength compared to the bulk value); and membrane 2# (down, model IDM) shows suppressed concentration polarization. Detailed calculation parameters are listed in Supporting Information Table S4.

Table 1. Comparison with commercial ion-exchange membranes. The tests are conducted in identical experimental setup and by mixing artificial seawater (0.5 M NaCl) and river water (0.01 M NaCl) through the testing membranes

membrane type	U_{OC} (mV)	I_{SC} (A/m^2)	P_{max} (W/m^2)	wet thickness (μm)	efficiency (%)	cation transference number
Nafion	99.0	13.2	0.33	20	49.3%	0.993
Ionsep	99.6	15.3	0.37	540	49.6%	0.996
CMI	99.1	14.2	0.40	320	49.3%	0.993
FKS	100.2	12.5	0.26	20	49.9%	0.999
IDM	73.2	215.7	3.46	64	37.3%	0.864

width, the ion selectivity of the IDM is not as high as those ion-exchange membranes (Table 1). Consequently, the open-circuit voltage produced by the IDM is about 25% lower than that obtained with the ion-exchange membranes. But, owing to the high ionic flux, the short-circuit current is more than one order higher. Therefore, the maximum power output from the IDM can be much higher than that from the ion-exchange membranes. This value is expected to be further increased by lowering the electrode/membrane distance.[43]

■ CONCLUSIONS

In conclusion, we report the use of membrane-scale nanofluidic heterojunctions for harvesting electric power from salinity gradient in natural waters. The ionic diode membrane comprises asymmetric heterojunctions between negatively charged mesoporous carbon (pore size ∼7 nm) and positively charged macroporous alumina (pore size ∼80 nm). The asymmetries in structure, chemical composition, and surface charge polarity lead to rectified ion transport through the meso/macro channels with distinctly high rectification ratio of about 450. Particularly in high-concentration electrolytes, or even in saturated solutions, the nanofluidic IDM preserves the surface-governed ion transport and keeps on rectifying. The selective and rectified ion transport through the nanofluidic heterojunctions facilitates the cation transport from the mesoporous carbon to the macroporous alumina. These features shed light on the salinity gradient power generation. When artificial seawater and river water are mixed through the IDM, substantially high power density of up to 3.46 W/m^2 is

dx.doi.org/10.1021/ja503692z | J. Am. Chem. Soc. 2014, 136, 12265−12272

obtained, which largely outperforms many commercial ion-exchange membranes.

The proof-of-concept demonstration of cation-selective IDM can be further extended to fabricate anion-selective counterpart by chemical modification approaches. The tandem IDM stacks are expected to construct high-performance reverse electrodialysis devices extracting energy from natural waters or synthetic solutions. The IDM represents a fundamentally novel nanofluidic structure to upgrade current ion-exchange membrane based salinity gradient power systems, and has implication for other membrane-based technology for water purification and desalination.

EXPERIMENTAL SECTION

Membrane Fabrication. First, a macroporous alumina film was coated with 10 w% solution of PMMA (ca. 550 000 in molecular weight) in acetone (Supporting Information Figure S2). After a drying period of 2 h at room temperature, it was heated at 200 °C for 5 h to ensure that the PMMA entered into the alumina pores (Supporting Information). The PMMA outside the MacroA was gently removed with sandpaper. Then, the film was coated with MesoC (FDU-16) precursor solution, which was presynthesized according to our previous work.[30] After evaporation-induced self-assembly in atmosphere for 3 h, the membrane was calcined at 450 °C for 3 h. At such high temperature, the residual PMMA was decomposed completely.

Electrical Measurements. The membranes were mounted in between the two halves of a custom-made electrochemical cell.[44] Then, 1.0 mL of KCl (or NaCl) electrolyte was injected into each half-cell. The current−voltage properties were recorded with a picoammeter/voltage source using a pair of Ag/AgCl electrodes. The working electrode was set on the MesoC side. Before the test, the membranes were immersed in ethanol/water (1:1 in volume ratio) solution to ensure the water permeation.[45] The measurement of short-circuit current and open-circuit potential is accomplished within 5 min. The testing electrolyte solutions are refreshed before each measurement (Supporting Information Figure S11). For comparison, four types of cation-exchange membrane, including Nafion (Dupont,), Ionsep (Iontech, China), CMI (Membrane International), and FKS (Fumtech, Germany), were tested in identical experimental conditions (Supporting Information).[46]

Model Calculation. The mechanism of the ionic rectification and the energy conversion is systematically analyzed by solving the steady-state ion concentration distribution inside the meso/macro-channels based on coupled Poisson and Nernst−Planck equations.[47−49] The simulation system contains two electrolyte reservoirs connected by a two-segment nanochannel composed of the MesoC and the MacroA parts (Supporting Information and Figure S5). To gain an affordable computation scale, we use a 4 nm-width cylindrical nanochannel array to simulate the mesochannels and a 60 nm-width nanochannel to simulate the macrochannels. The geometric parameters are estimated from the SEM observations. The outer and inner surface of the MesoC and MacroA channels are charged. The model simulations are carried out within the Comsol Multiphysics environment using the "electrostatics (Poisson equation)" and "Nernst-Planck without Electroneutrality" modules. Details of the model parameters are summarized in Tables S2−S4 (Supporting Information).

ASSOCIATED CONTENT

Supporting Information

Details of fabrication and characterization, electrical measurement, pH-dependent ionic rectification, calculation of energy conversion efficiency, comparison with ion-exchange membranes, model calculation and parameters, permeation of charged fluorescent dyes, time-dependence of the diffusion current, and calibration of electrode potential. This material is available free of charge via the Internet at http://pubs.acs.org.

AUTHOR INFORMATION

Corresponding Authors

wguo@iccas.ac.cn
dyzhao@fudan.edu.cn
jianglei@iccas.ac.cn

Notes

The authors declare no competing financial interest.

ACKNOWLEDGMENTS

Dr. Mei-rong Liu and Ms. Li-ping Ding (Center for Physiochemical Analysis and Measurement, ICCAS) is acknowledged for technical help. The model calculation benefits from the discussion with Dr. Wen Ma (Beckman Institute, UIUC). This work is financially supported by the National Research Fund for Fundamental Key Projects (2011CB935700, 2013CB934104), the National Natural Science Foundation of China (21103201, 11290163, 91127025, 21121001). The Chinese Academy of Sciences is gratefully acknowledged under the Key Research Program of the CAS (KJZD-EW-M01).

REFERENCES

(1) Pacala, S.; Socolow, R. *Science* **2004**, *305*, 968.
(2) Logan, B. E.; Elimelech, M. *Nature* **2012**, *488*, 313.
(3) Shannon, M. A.; Bohn, P. W.; Elimelech, M.; Georgiadis, J. G.; Marinas, B. J.; Mayes, A. M. *Nature* **2008**, *452*, 301.
(4) Post, J. W.; Hamelers, H. V. M; Buisman, C. J. N. *Environ. Sci. Technol.* **2008**, *42*, 5785.
(5) Xu, J.; Sigworth, F. J.; LaVan, D. A. *Adv. Mater.* **2010**, *22*, 120.
(6) Guo, W.; Tian, Y.; Jiang, L. *Acc. Chem. Res.* **2013**, *46*, 2834.
(7) Pattle, R. E. *Nature* **1954**, *174*, 660.
(8) Loeb, S.; Van Hessen, F.; Shahaf, D. *J. Membr. Sci.* **1976**, *1*, 249.
(9) Weinstein, J. N.; Leitz, F. B. *Science* **1976**, *191*, 557.
(10) Post, J. W.; Veerman, J.; Hamelers, H. V. M; Euverink, G. J. W.; Metz, S. J.; Nymeijer, K.; Buisman, C. J. N. *J. Membr. Sci.* **2007**, *288*, 218.
(11) Achilli, A.; Childress, A. E. *Desalination* **2010**, *261*, 205.
(12) Schoch, R. B.; Han, J. Y.; Renaud, P. *Rev. Mod. Phys.* **2008**, *80*, 839.
(13) Xu, J.; Lavan, D. A. *Nat. Nanotechnol.* **2008**, *3*, 666.
(14) Guo, W.; Cao, L. X.; Xia, J. C.; Nie, F. Q.; Ma, W.; Xue, J. M.; Song, Y. L.; Zhu, D. B.; Wang, Y. G.; Jiang, L. *Adv. Funct. Mater.* **2010**, *20*, 1339.
(15) Kim, D. K.; Duan, C.; Chen, Y. F.; Majumdar, A. *Microfluid. Nanofluid.* **2010**, *9*, 1215.
(16) Siria, A.; Poncharal, P.; Biance, A. L.; Fulcrand, R.; Blase, X.; Purcell, S. T.; Bocquet, L. *Nature* **2013**, *494*, 455.
(17) Fan, R.; Huh, S.; Yan, R.; Arnold, J.; Yang, P. *Nat. Mater.* **2008**, *7*, 303.
(18) Sparreboom, W.; van den Berg, A.; Eijkel, J. C. T. *Nat. Nanotechnol.* **2009**, *4*, 713.
(19) Jiang, Y.; Liu, N.; Guo, W.; Xia, F.; Jiang, L. *J. Am. Chem. Soc.* **2012**, *134*, 15395.
(20) Guo, W.; Cheng, C.; Wu, Y.; Jiang, Y.; Gao, J.; Li, D.; Jiang, L. *Adv. Mater.* **2013**, *25*, 6064.
(21) Dekker, C. *Nat. Nanotechnol.* **2007**, *2*, 209.
(22) van der Heyden, F. H. J.; Bonthuis, D. J.; Stein, D.; Meyer, C.; Dekker, C. *Nano Lett.* **2007**, *7*, 1022.
(23) Xia, F.; Guo, W.; Mao, Y.; Hou, X.; Xue, J.; Xia, H.; Wang, L.; Song, Y.; Ji, H.; Ouyang, Q.; Wang, Y.; Jiang, L. *J. Am. Chem. Soc.* **2008**, *130*, 8345.
(24) Yan, R. X.; Liang, W. J.; Fan, R.; Yang, P. D. *Nano Lett.* **2009**, *9*, 3820.
(25) Guan, W.; Fan, R.; Reed, M. A. *Nat. Commun.* **2011**, *2*, 506.
(26) Gao, J.; Guo, W.; Geng, H.; Hou, X.; Shuai, Z.; Jiang, L. *Nano Res.* **2012**, *5*, 99.

(27) Davis, M. E. *Nature* **2002**, *417*, 813.
(28) Wan, Y.; Yang, H.; Zhao, D. *Acc. Chem. Res.* **2006**, *39*, 423.
(29) Yamauchi, Y.; Kuroda, K. *Chem.—Asian J.* **2008**, *3*, 664.
(30) Feng, D.; Lv, Y.; Wu, Z.; Dou, Y.; Han, L.; Sun, Z.; Xia, Y.; Zheng, G.; Zhao, D. *J. Am. Chem. Soc.* **2011**, *133*, 15148.
(31) Vogt, B. D.; Chavez, V. L.; Dai, M.; Arreola, M. R. C.; Song, L.; Feng, D.; Zhao, D.; Perera, G. M.; Stein, G. E. *Langmuir* **2011**, *27*, 5607.
(32) Cheng, L. J.; Guo, L. J. *Chem. Soc. Rev.* **2010**, *39*, 923.
(33) Siwy, Z. S. *Adv. Funct. Mater.* **2006**, *16*, 735.
(34) Stein, D.; Kruithof, M.; Dekker, C. *Phys. Rev. Lett.* **2004**, *93*, 035901.
(35) He, Y.; Gillespie, D.; Boda, D.; Vlassiouk, I.; Eisenberg, R. S.; Siwy, Z. S. *J. Am. Chem. Soc.* **2009**, *131*, 5194.
(36) Constantin, D.; Siwy, Z. S. *Phys. Rev. E* **2007**, *76*, 041202.
(37) Cao, L.; Guo, W.; Wang, Y.; Jiang, L. *Langmuir* **2012**, *28*, 2194.
(38) Vlassiouk, I.; Smirnov, S.; Siwy, Z. *ACS Nano* **2008**, *2*, 1589.
(39) Cervera, J.; Alcaraz, A.; Schiedt, B.; Neumann, R.; Ramírez, P. *J. Phys. Chem. C* **2007**, *111*, 12265.
(40) Długołęcki, P.; Gambier, A.; Nijmeijer, K.; Wessling, M. *Environ. Sci. Technol.* **2009**, *43*, 6888.
(41) Vlassiouk, I.; Smirnov, S.; Siwy, Z. *Nano Lett.* **2008**, *8*, 1978.
(42) Okada, T.; Xie, G.; Gorseth, O.; Kjelstrup, S.; Nakamura, N.; Arimura, T. *Electrochim. Acta* **1998**, *43*, 3741.
(43) Vermaas, D. A.; Saakes, M.; Nijmeijer, K. *Environ. Sci. Technol.* **2011**, *45*, 7089.
(44) Guo, W.; Xia, H.; Xia, F.; Hou, X.; Cao, L.; Wang, L.; Xue, J.; Zhang, G.; Song, Y.; Zhu, D.; Wang, Y.; Jiang, L. *ChemPhysChem* **2010**, *11*, 859.
(45) Zhou, Y.; Guo, W.; Jiang, L. *Sci. China: Phys., Mech. Astron.* **2014**, *57*, 836.
(46) Veerman, J.; de Jong, R. M.; Saakes, M.; Metz, S. J.; Harmsen, G. J. *J. Membr. Sci.* **2009**, *343*, 7.
(47) Liu, Q.; Wang, Y.; Guo, W.; Ji, H.; Xue, J.; Ouyang, Q. *Phys. Rev. E* **2007**, *75*, 051201.
(48) White, H. S.; Bund, A. *Langmuir* **2008**, *24*, 2212.
(49) Cao, L.; Guo, W.; Ma, W.; Wang, L.; Xia, F.; Wang, S.; Wang, Y.; Jiang, L.; Zhu, D. *Energy Environ. Sci.* **2011**, *4*, 2259.